Carbon molecular-sieve membranes developed from a Tröger's base polymer and possessing superior gas-separation performance

Zhongde Dai[1,2,3], Hongfang Guo[1,2,3,4], Jing Deng[5*], Liyuan Deng[6*],

Jiaqi Yan[7†], and Richard J. Spontak[7,8]

[1]School of Carbon Neutrality Future Technology, Sichuan University, Chengdu 610065, China

[2]National Engineering Research Centre for Flue Gas Desulfurization, Chengdu 610065, China

[3]Carbon Neutral Technology Innovation Center of Sichuan, Chengdu 610065, China

[4]College of Architecture and Environment, Sichuan University, Chengdu 610065, China

[5]ALTR FLTR Inc., Phoenix, Arizona, 85034, USA

[6]Department of Chemical Engineering, Norwegian University of Science and Technology Trondheim, 7491, Norway

[7]Department of Chemical & Biomolecular Engineering, North Carolina State University, Raleigh, NC 27695, USA.

[8]Department of Materials Science & Engineering, North Carolina State University, Raleigh, NC 27695, USA

Abstract:

Carbon molecular-sieve membranes possess tremendous practical advantages over unary polymer membranes by providing high gas-separation performance levels, coupled with excellent mechanical and chemical stability. Improving their overall effectiveness greatly expands the competitiveness of this class of membranes. In the present study, carbon membranes are fabricated from a Tröger's base polymer as the precursor. By optimizing the carbonization conditions, the gas-separation performance of the resultant membranes are significantly enhanced. Under optimized conditions, a H_2 permeability of up to 1135 Barrer is achieved, with a corresponding H_2/CH_4 selectivity of 1170 and a CO_2/CH_4 selectivity of 238. While increasing the operating temperature slightly reduces the selectivity, it still remains in the high-separation region. Overall, the measured separation performance levels for H_2-related separations, *i.e.*, H_2/CH_4, H_2/N_2 and H_2/CO_2, all substantially exceed the Robeson upper bound. Moreover, the CO_2/CH_4 separation efficacy

---

[*] To whom correspondence should be addressed (e-mail: jing@altrfltr.com)
[†] Current address: Kraton Innovation Center, Kraton Corporation, Houston, TX 77084.

also lies above the 2019 upper bound, indicating that the carbon membranes developed in the present work are versatile and promising for many different gas-separation applications.

Highlights:

* Carbon molecular-sieve membranes possessing superior gas-separation performance levels were fabricated from a Tröger's base polymer;

* Structural features of the membranes generated here were characterized by X-ray diffraction (XRD) and small-angle X-ray scattering (SAXS);

* With these membranes, H_2 permeabilities have been measured up to 1135 Barrer, along with a H_2/CH_4 selectivity of 1170;

* The carbon molecular-sieve membranes under investigation exhibit superior H_2 and CO_2 separation effectiveness beyond the selectivity-permeability upper bound.

TOC Graphic:
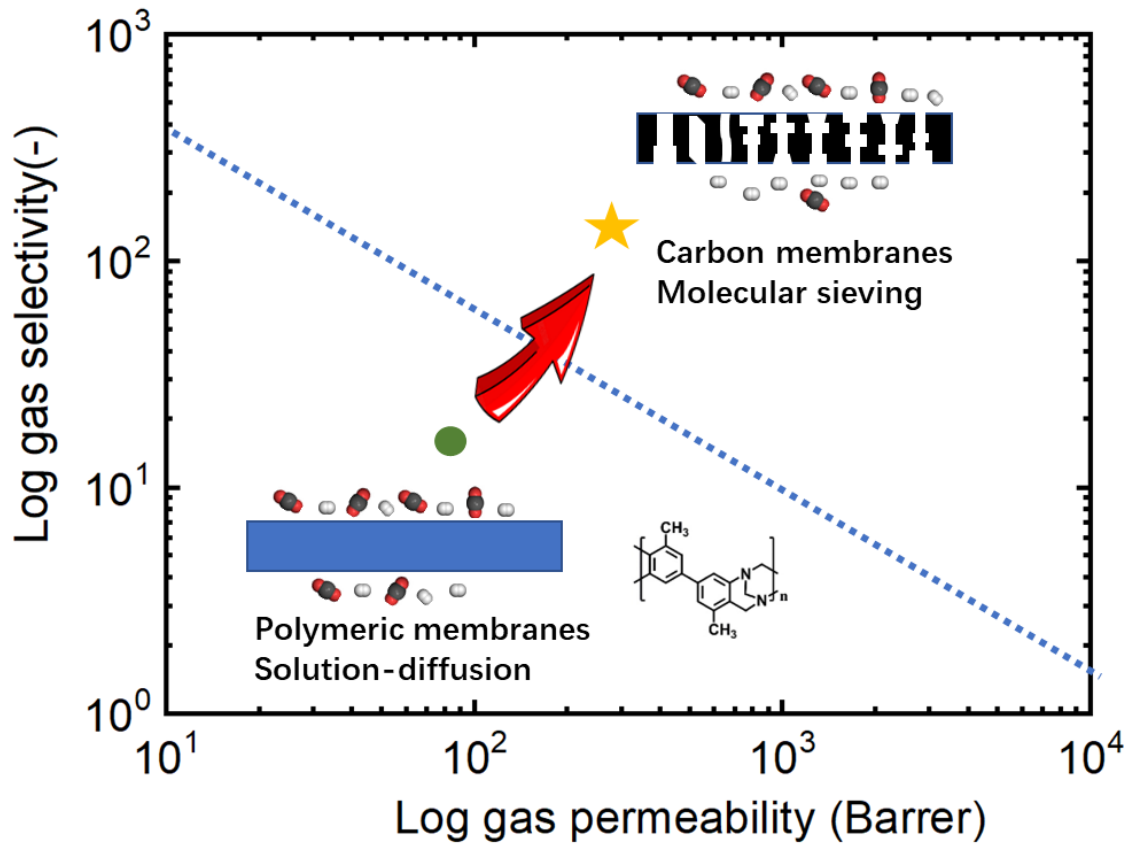
1. Introduction

Notable for high energy efficiency [1], membrane technology, especially designed for gas separations, has become increasingly important for both extraction and purification purposes. An example of this two-prong objective focuses on the removal of CO_2 (*i*) as a greenhouse compound from flue gas to protect the environment and (*ii*) as a diluent from natural resources (*e.g.*, CH_4 and H_2) to improve fuel efficiency or chemical purity. The global market associated with gas-separation membranes is estimated to be ~ \$822 million, with a predicted annual growth of 5.6% in the following period [2]. Despite the excellent processability and relative low cost of many polymer gas-separation membranes, they generally suffer from the trade-off between permeability (thickness- and pressure-normalized flux) and selectivity, along with plasticization in the presence of gases such as CO_2. The latter is caused by the sorption of penetrant molecules in polymers, which enlarges the free volume between polymer chains to accommodate more penetrant, resulting in a concurrent increase in permeability and decrease in selectivity. While most polymer gas-separation membranes are fabricated from single polymers with or without additives such as zeolites [3] or metal-organic frameworks (MOFs) [4] , recent advances in chemical surface functionalization [5] have also been reported to greatly enhance the gas-separation efficacy of carbon-capture membranes based on homopolymers such as polydimethylsiloxane and polytetrafluoroethylene (amorphous form).

As an alternative to polymer membranes, carbon membranes are fabricated by pyrolyzing polymers at high temperature (typically 500-1000 °C) under oxygen-free conditions so that the polymers decompose and most of the non-carbonaceous elements are removed [6]. The carbon residue forms (sub)nanoscale pores capable of differentiating penetrant molecules on the basis of their size and shape. Since this mechanism is referred to as molecular sieving, these membranes are classified as carbon molecule sieves (CMSs). Unlike their polymer precursors, the rigid carbon network in CMS possesses is relatively immobile, which makes these membranes remarkably plasticization-resistant. In addition, CMS membranes can operate under harsh conditions such as high temperatures (> 100 °C) that are unsuitable for most polymer membranes. The pores present in CMS are categorized

according to size: ultramicropores (< 7 Å), which tend to govern gas-separation effective-ness, are connected by micropores (7~20 Å) [7-9]. The size and shape of ultramicropores play important roles in the separation ability of CMS, and the population of micropores determines its permeability [10-12]. The details of these physical factors are sensitively influenced by the pyrolysis conditions (*e.g*., temperature, atmosphere and heating rate), as well as the chemical constitution and (micro)structure of the precursor polymer [13].

Numerous studies of CMS membranes have related pyrolysis conditions to gas-separation performance, whereas much less attention has focused on precursor selection. Since the chemical and physical structure of the precursor polymer impacts the complex chemical reactions during pyrolysis and therefore the final CMS nanostructure, the choice of precursor polymer can be used as an independent knob to tailor gas-separation performance [14, 15]. Several studies have reported that CMS membranes derived from glassy polymers possessing relatively high fractional free volume are generally more permeable relative to those fabricated from glassy polymers having similar chemical structure but lower fractional free volume [16-19]. One well-known example of this phenomenon is CMS prepared from 4,4'-(hexafluoroisopropylidene)diphthalic anhydride:3,3'-4,4'-biphenyl tetracarboxylic dianhydride-2,4,6-trimethyl-1,3-phenylene diamine [6FDA: BPDA-DAM (1:1)] polyimide, which exhibits greater gas permeability compared to Matrimid®, a less permeable polyimide precursor, under the same pyrolysis and test conditions [20-23]. The characteristic high free volume tends to be retained, as evinced by higher gas diffusivity, greater gas sorption uptake (due to more cavities), and a larger population of ultramicropores [20-24]. Additional efforts have likewise observed a direct dependence of CMS transport properties on relevant characteristics of the polyimide precursor [16, 17, 19, 25, 26], especially in the case of stiff-chain polymers [27-29]. This leads to a accepted rule of thumb: an increase in the rigidity of the precursor chain is accompanied by an increase in the gas permeability of the corresponding CMS. One explanation for this is that stiff chains inefficiently pack, which, combined with bulky aromatic groups, could preserve the original narrow cavities during pyrolysis.

Equally important, increasing pyrolysis temperature generates polyimide-based CMS with similar performance levels, since polyimides form similar microstructures in the

resultant CMS [20-23]. Some concern has recently been raised [28], however, regarding the possibility of relatively flexible chains leading to pore collapse during pyrolysis. While this discussion is limited to CMS precursors derived exclusively from polyimides, a broader range of suitable candidates possessing (*i*) rigid chains and high free volume, (*ii*) excellent heat resistance and a high glass transition temperature and (*iii*) reasonable availability should be considered. In the present study, the candidate library is extended to include another high free-volume polymer, namely, Tröger's base (TB) polymer [30, 31]. Here, CMS membranes have been fabricated from TB polymer at various carbonization temperatures, and the effect of carbonization temperature on the microstructure and gas-transport properties of resulting CMS membranes has been systemically evaluated by X-ray diffraction (XRD), small-angle X-ray scattering (SAXS), and pure-gas permeation using H_2, CO_2, N_2, and CH_4. Furthermore, the most promising CMS membrane is selected to elucidate the influence of operating temperature and pressure on molecular transport.

2. Experimental

2.1 Materials

o-Tolidine, dimethoxymethane (DMM), trifluoroacetic acid (TFA), ammonium hydroxide solution (28%) and *N*-methylpyrrolidone (NMP) were purchased from Sigma-Aldrich (Darmstadt, Germany), whereas methanol was bought from VWR (Oslo, Norway). All these chemicals were used as-received without further purification. The H_2, N_2, CH_4, and CO_2 gases (at least 99.999% pure) employed in the permeation tests, as well as Ar to provide an inert atmosphere during pyrolysis, were obtained from AGA A/S (Oslo, Norway).

2.2 Polymer preparation

The TB polymer was synthesized in-house as the CMS precursor according to the detailed procedure that was previously provided [30]. In short, 20 g *o*-tolidine and 36 g DMM were mixed and stirred in a three-necked flask maintained at 0 °C under an inert (N_2) atmosphere. After thorough mixing, 200 mL TFA were added dropwise into the solution over the course of 30 min, followed by warming to ambient temperature. The reaction,

yielding the polymer whose chemical structure is displayed in **Scheme 1**, was terminated after 48 h by slowly adding an excess of 5 wt% aqueous NH_4OH solution into the mixture. The precipitated solid was collected and washed in deionized (DI) water until the pH reached 7, and then dried under vacuum at 80 °C for 12 h. To remove residual reactant and short chains in a purification step performed at least twice, the polymer was dissolved in NMP at a concentration of ~10 wt% and then re-precipitated in methanol. Finally, the TB polymer was dried at 80 °C under vacuum for an additional 12 h and stored until needed. Films were produced by dissolving the TB polymer in NMP and casting the solution onto a clean glass plate where it was evened with a casting knife (PA-4302, BYK-CHEMIE GMBH, Germany). The cast solution was transferred to a vacuum oven, where the solution was heated to 80 °C under vacuum for 24 h to completely remove the solvent.
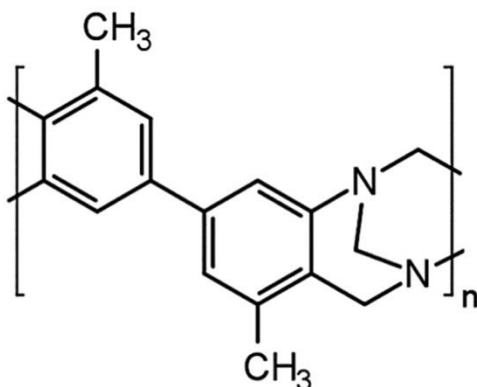
Scheme 1. Chemical structure of the TB polymer precursor synthesized in this study.

2.3 Membrane carbonization

The dried, flat TB polymer film was cut into ~5 cm squares, and each square was sandwiched between two porous metal dishes. The assemblies were placed in a tubular furnace (Carbolite Gero Ltd), which was first evacuated to remove atmospheric gases and then backfilled with Ar prior to increasing the temperature at a rate of 10 °C/min to the desired carbonization temperature. Pyrolysis temperatures exceeded the decomposition temperature of the precursor TB polymer, as previously measured by thermogravimetric

analysis [30], but consistently remained below 1000 °C. The carbonization period was maintained at 2 h, followed by quiescent cooling. During the entire carbonization process, the Ar flow rate was maintained at 20 mL/min to ensure the absence of O_2. The resulting carbonized TB membranes are hereafter designated as CTB-T_c, where T_c denotes the carbonization temperature (expressed in °C). All CMS membranes were tested immediately to avoid aging [32-34]. The thickness of membranes ranged from 40 to 50 µm, as determined more than 10 times for each sample on an ABS Digimatic Indicator (Mitutoyo, Suzhou, China).

2.4 Material characterization

X-ray diffraction (XRD) was performed on a Bruker D8 Advance X-ray diffractometer equipped with a Cu source to assess the crystallographic details of the precursor TB polymer membranes and corresponding CMS membranes. In conjunction with the acquired scattering profiles, Bragg's law yielded the average d-spacing (d) inside each membrane according to

$$d = 2\lambda/sin\theta \tag{1}$$

where λ is the characteristic wavelength of the Cu source (1.54 Å), and θ represents the angle associated with each scattering peak. Similarly, small-angle X-ray scattering (SAXS) was conducted at the Advanced Photon Source (Argonne National Laboratory). Scattered photons were collected on a 2-D detector and azimuthally integrated to yield scattering profiles in which intensity is a function of scattering vector (q), where q = $(4\pi/\lambda)sin\theta$ and θ is half the scattering angle. Raman spectra of the membranes were acquired on a Horiba LabRAM HR spectrometer at a laser wavelength of 532 nm. The wavenumber range examined was 400 to 2000 cm^{-1}. Surface topologies of the CMS membranes were surveyed by scanning electron microscopy (SEM) performed on a field-emission FEI Nova NanoSEM450 microscope operated at an accelerating voltage of 5 kV and equipped with a probe (Azteclive and Ultim Max, Oxford) for energy dispersive spectroscopy (EDS). The thermal stability of the membranes was measured by thermogravimetric analysis (TGA) on a NETZSCH STA 449 F3 Jupiter testing station at a heating rate of 10 °C/min from ambient temperature to 1000 °C under a N_2 atmosphere.

2.5 Transport measurements

Membrane transport properties were evaluated by single-gas permeation tests according to the constant-volume variable-pressure protocol. Samples were first attached to the membrane cell with hollow alumina tape, and the edge between the membrane and alumina tape was sealed by fast-cure glue (Locitite EA 3090). The permeation cell was evacuated for at least 6 h to remove gases inside the system. A specific gas was fed at a desired pressure into the upstream side of membrane as the pressures of the upstream and downstream sides were recorded by Labview. Tests were terminated once permeation reached steady state. The gases were tested in the order of H_2, N_2, CH_4, and CO_2 to avoid any potential plasticization complications due to CO_2. The operating temperature was adjusted by a temperature control system attached to the permeation rig. Gas permeability (P) values were calculated from

$$P = \left[\left(\frac{dp_d}{dt} \right)_{t \to \infty} - \left(\frac{dp_d}{dt} \right)_{\text{leak}} \right] \cdot \frac{V_d}{ART} \cdot \frac{1}{(p_u - p_d)} \tag{2}$$

Here, p_u and p_d refer to the upstream and downstream pressures, respectively, t is time, V_d represents the downstream volume, A constitutes the effective membrane area for permeation, R and T denote the gas constant and absolute temperature, respectively, and l is the average membrane thickness discerned from at least 10 measurements of each membrane. The leakage rate $(^{dp_d}/_{dt})_{\text{leak}}$ is the rate at which the downstream pressure increases in a leakage test (2 bar N_2), which was constant for all membrane samples, and the permeation rate (dP/dt) of all membranes examined here was orders of magnitude higher than the leakage rate. Since the feed pressure was also held constant during permeation tests and the downstream pressure was < 100 mbar, the thermodynamic driving force ($p_u - p_d$) remained unchanged. Permeability data reported here reflects the average of at least 2 individual samples with a relative error of below 10%. The ideal selectivity of gas A relative to gas B ($\alpha_{A/B}$) was calculated as their permeability ratio:

$$\alpha_{A/B} = \frac{P_A}{P_B} \tag{3}$$

If permeation obeys the van 't Hoff relationship over a relatively narrow temperature range, the permeability of a single gas is expected to exhibit Arrhenius thermal behavior, *viz.*,

$$P = P_0 e^{-\frac{E_p}{RT}} \tag{4}$$

where P_0 is a pre-exponential factor and E_P is the activation energy of permeation.

3. Results and Discussion

3.1 Thermogravimetric analysis

The TB polymer has been analyzed by TGA to ascertain its thermal stability, as illustrated in **Figure 1**. The precipitous decomposition temperature of the TB polymer occurs between ~400 and 450 °C, and a little less than 80% of the mass remains at 1000 °℃, confirming excellent thermal stability. In addition, due to the inherent advantages of its rigid-chain structure, subsequently prepared CMS membranes have sufficient mechanical strength, in which case our CTB materials possess promising development prospects.
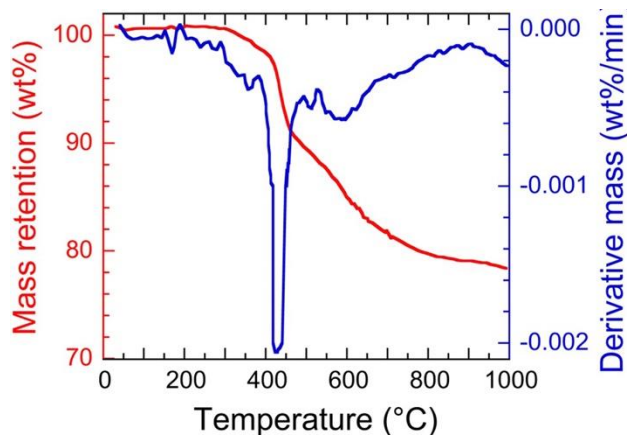

Figure 1. TGA (red) and DTG (blue) data acquired from the TB polymer precursor at a heating rate of 10 °C/min under N_2.

3.2 X-ray diffraction analysis

The TB polymer precursor and several carbonized membranes have been analyzed by XRD to ascertain their structural characteristics. Representative XRD scattering profiles are presented in **Figure 2** and reveal a clear structural progression as the carbonization temperature is increased. The TB polymer precursor displays a broad peak in the range 5-

10

30° 2θ with a principal peak positioned at 12.7° (with a corresponding *d*-spacing of 6.96 Å) and a broad shoulder that extends up to ~30°. This feature is consistent with the expected [19] amorphous state of the TB polymer. Once the TB polymer is pyrolyzed to form CMS, two well-defined peaks develop near 23° and 44° as the carbonization temperature is increased from CTB-500 at 500 °C to CTB-700 at 700 °C. The peak near 44° is close to the characteristic (100) plane of graphite arising from the 2.10 Å distance between parallel hexagonal graphite units [35, 36], indicating an increase in the presence of graphite-like structure in the CTB membranes with increasing carbonization temperature. The other peak relates to the signature (002) plane in graphite at 3.35 Å, which corresponds to the interlayer space between two adjacent graphite layers [36-38], but at slightly lower position, indicating a larger averaged *d*-spacing (see **Table 1**). This difference signifies that the graphite structure formed during carbonization is not ideal. Hence, defects (*e.g*., holes or cracks) likely exist on single graphite layers or residual polymer chains/fragments remain after carbonization, thereby increasing the interlayer distance [21, 39].

The broad principal peak of the TB precursor membrane is no longer discernible at carbonization temperatures of 600 °C and completely disappears at 700 °C, confirming the temperature-dependent transformation from polymer chain packing to a more closely-packed graphitic structure, as further evidenced by the reduction in *d*-spacing in the CTB membranes relative to the TB polymer precursor in **Table 1**. A comforting feature of the data included in **Figure 2** is that the XRD profiles acquired at 500, 600 and 700 °C exhibit a systematic evolution with regard to the shapes and positions of the peaks associated with graphitic spacings. In contrast, the scattering profile collected from the CTB-650 material produced at 650 °C is virtually identical to the one corresponding to CTB-600, suggesting that the temperature difference of 50 °C has little impact on structure development when the time of carbonization is held constant (2 h). We hasten to point out that these results do not confirm that the CTB membranes generated here have been fully transformed into graphite. Rather, their actual structure is anticipated to represent a combination of flexible chain segments embedded within a graphite-like structure [22, 40, 41]. Under the carbonization conditions employed in this study, only the CTB-700 membrane comes closest, from the crystallographic data in **Figure 2**, to resembling pure graphite. At higher

carbonization temperatures or longer carbonization times, we suspect that these CTB membranes will become increasingly graphitic.
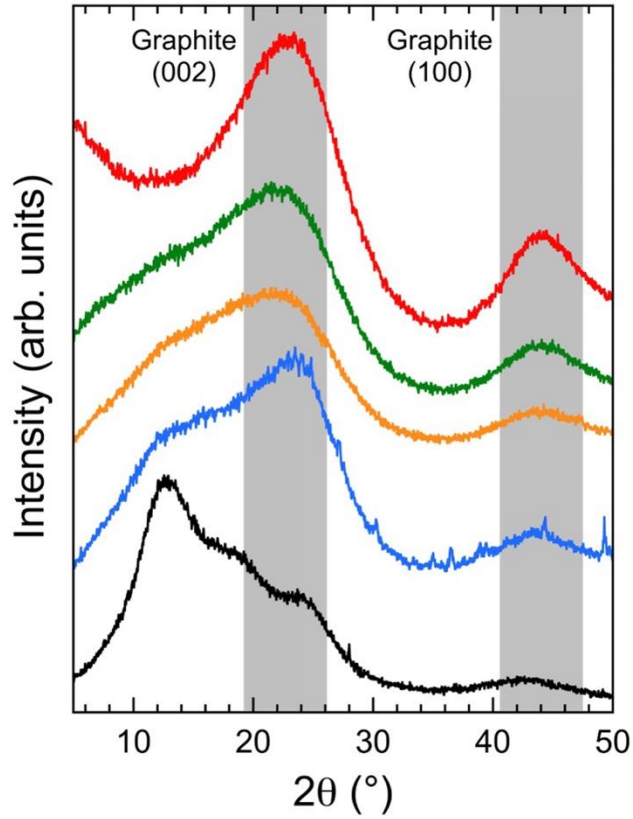

Figure 2. XRD profiles of CTB membranes fabricated at several temperatures, as well as the neat TB polymer precursor – CTB-700 (red), CTB-650 (green), CTB-600 (orange), CTB-500 (blue), and precursor (black). The shaded regions identify the positions corresponding to the (002) and (100) planes of graphite.

Table 1. Peak positions and corresponding *d*-spacings of graphite and CTB membranes carbonized at several temperatures.

Material	$2\theta_{002}$ (°)	d_{002} (Å)	$2\theta_{100}$ (°)	d_{100} (Å)
Graphite[a]	—	3.35	—	2.10
CTB-700	23.05	3.85	43.89	2.06
CTB-650	22.33	3.98	44.30	2.04
CTB-600	21.88	4.06	44.00	2.05
CTB-500	22.27	3.99	—	—

3.3 Small-angle X-ray scattering analysis

The corresponding SAXS profiles obtained by azimuthal integration of 2D scattering patterns acquired from the same four CTB membranes are displayed in **Figure 3a** and reveal no correlation peaks indicative of long-range order, implying that the pore structure is randomly arranged. An enlargement of the low-q region replotted to facilitate a Guinier analysis, with log(intensity) shown as a function of q^2, is provided in **Figure 3b**. In most cases, Guinier analyses are applied to biphasic systems composed of discrete particulates dispersed in a continuous (often liquid) matrix. Because the CTB membranes consist of pores randomly positioned within a solid matrix, the scattering behavior is considered to be comparable if not identical. Two features of **Figure 3b** warrant discussion. First, the data presented in the form of log(intensity) $\sim -R^2q^2$, where R is the radius of the scattering object/pore, do not conform to a linear fit, which, in the case of particulates, suggests aggregation. In the present system, however, aggregated particulates could be construed as loosely equivalent to highly connected pores in agreement with the envisaged structure of CMS membranes. The second characteristic is that the scattering intensity increases with increasing T_c in the order CTB-500 < CTB-600 $\approx$ CTB-650 < CTB-700. An increase in scattering in the low-q region is attributed to an increase in the population or size (or both) of micropores. On the basis of this finding, we propose that the permeability of the smallest inert gas examined here (H_2) should be the highest in the CTB-700 membrane.

In addition, since the SAXS profiles of the CTB600 and CTB650 membranes are nearly identical in **Figure 3b**, these two materials are expected to have comparable pore morphologies, which is qualitatively consistent with the XRD results discussed with respect to **Figure 2**. Additional insight can be gleaned from the high-q region provided in **Figure 3c**, wherein log(intensity) is displayed as a function of log(q) so that the scaling exponent n in the expression (intensity $\sim q^{-n}$) can be determined from regression analysis of the data. This scattering region, referred to as the Porod regime, provides information regarding the sharpness of the interface between coexisting features differing in electron density (in this case, the pores within the CMS matrix). A sharp interface exists when $n =$

4, whereas the interface is diffuse if $n < 4$. Values of n extracted from the results in **Figure 3c** increase slightly, but systematically, from 0.30 for CTB500 to 0.46 for CTB700, indicating that the pores in these CMS membranes are not sharply delineated from the carbon matrix. This scenario reflects the nature of the precursor and confirms our earlier conclusion drawn from the XRD data in **Figure 2**, namely, the membranes generated under the conditions employed here are not fully graphitic, but rather exist as a hybrid of graphite and residual polymer. Our observation that n increases with increasing T_c further implies that the pores become more sharply defined as the carbonization temperature (or presumably time) yields a more graphitic CMS. Since well-defined pores without diffusive obstruction are likely to assist molecular transport, the CTB-700 membrane is anticipated to exhibit the highest selectivity of H_2 with respect to the other gases tested here.

3.4 Raman spectroscopic analysis

Raman spectroscopy is widely used to provide chemical information regarding the ordered and disordered characteristics of CMS membranes [42]. In this study, the Raman spectra included in **Figure 4** display the typical G band (located at ~1600 cm^{-1} and indicative of ordered graphite) and a D band (located at ~1380 cm^{-1} and indicative of defective graphite) of CMS membranes. The G band is assigned to the characteristic peak of the ideal graphitic vibration mode (with E_{2g}-symmetry). As T_c increases, the peak
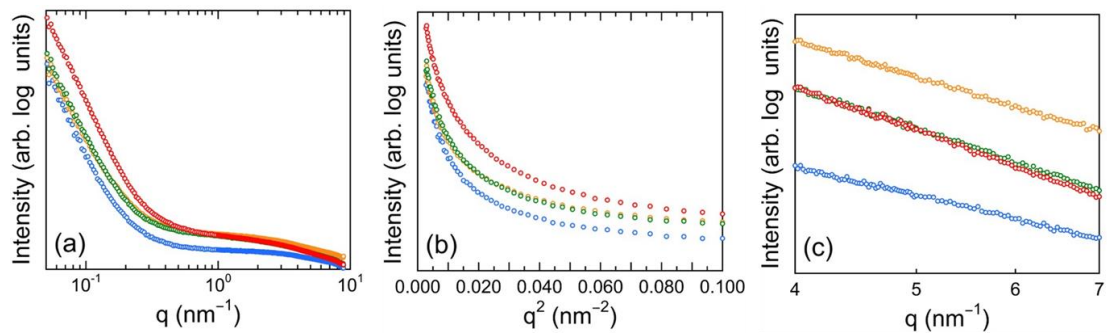
14

Figure 3. (a) SAXS results of CTB membranes – CTB-700 (red), CTB-650 (green), CTB-600 (orange), CTB-500 (blue) – prepared at different carbonization temperatures. (b) Guinier analysis of the same CTB membranes at low-q values. (c) Porod analysis of the same CTB membranes at high-q values.

intensity of G the band likewise increases, resulting in a reduced D/G intensity ratio. A decrease in this ratio is associated with smaller and/or fewer defects reflecting incomplete carbonization of the TB polymer precursor and the presence of residual polymer chains or fragments, and a correspondingly higher degree of graphitic order in carbonaceous materials [43]. These results are in favorable agreement with reports [27] of other CMS membranes, as well as the XRD results provided in **Figure 2**. In addition, the apparent increase in the level of graphitization in the present CMS membranes obtained at higher pyrolysis temperatures indicates that the CTB-700 and CTB-750 membranes should possess the greatest degree of gas selectivity, which coincides with the same expectation based on the SAXS analyses related to **Figure 3**.
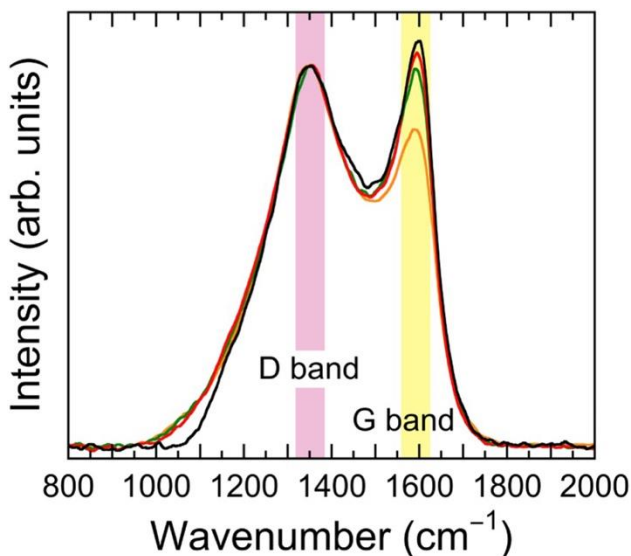

Figure 4. Raman spectra of CTB membranes – CTB-750 (black), CTB-700 (red), CTB-650 (green), and CTB-600 (orange) – prepared at different carbonization temperatures. The G and D bands corresponding to ordered and defective graphite are also labeled.

3.5 Electron microscopy analysis

Membrane surface topologies have been examined by SEM/EDS, and representative secondary-electron images and associated carbon maps are displayed in **Figure 5**. The TB polymer precursor pictured in **Figure 5a** appears relatively featureless, whereas submicron holes presumably associated with the carbonization process are prevalent on the surface of each membrane in **Figures 5b-d**. Surface holes often reflect outgassing due to, for example,

solvent evaporation or organic decomposition. While the carbonization temperature has little influence on the size or number density of these holes, subtle differences are visible in these images. In **Figure 5b**, many of the hole-like features appear to be diffuse and possibly sub-surface on the CTB-600 membrane, which is consistent with the notion that the holes originate as internal bubbles that can become trapped as volatile organic species outgas during carbonization. These diffuse and/or sub-surface features are, for the most part, absent in the CTB-650 membrane in **Figure 5c**, and the surface holes appear more sharply defined. The holes seem to possess the sharpest boundaries, and virtually no sub-surface features exist, on the CTB-700 membrane in **Figure 5d**. The carbon X-ray maps provided in **Figure 5** further reveal that the carbonaceous regions comprising the CMS membrane surfaces become increasingly more uniform (with fewer low-carbon dark regions) as T_c is increased, whereas the carbon map of the TB polymer precursor exhibits considerable spatial intensity variation. This trend is consistent with results from thermogravimetric analysis [44], which reveals that the nitrogen moieties of the polymer
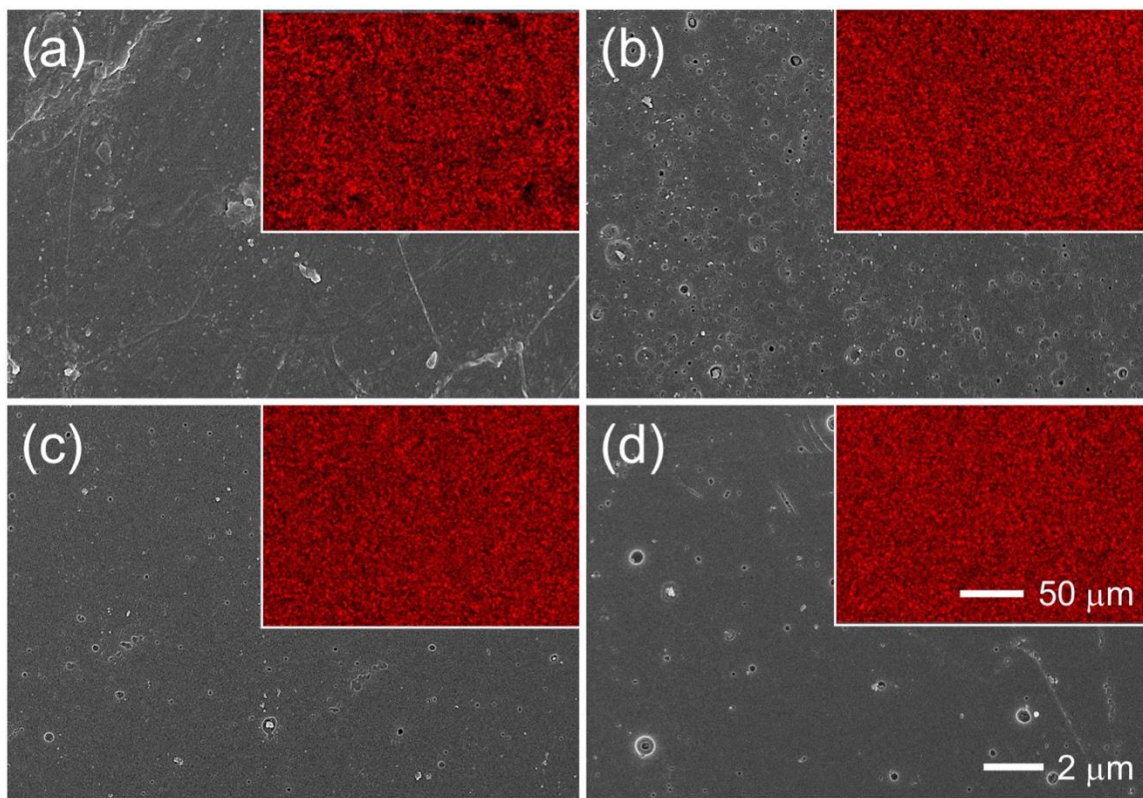

Figure 5. SEM surface images of (a) the TB polymer precursor, (b) the CTB-600 membrane, (c) the CTB-650 membrane, and (d) the CTB-700. The scalebar in (d) applies to all the images. Corresponding carbon X-ray maps are included as insets, and the scalebar in the inset in (d) applies to all the insets.

chains are the least thermally stable and decompose at relatively low temperatures. The micropores and ultramicropores expected in these CMS membranes most likely measure less than 1 nm and are beyond the resolution limit of the microscope employed. Cross-section SEM observation was conducted on the sample in **Figure 5**, and the results were shown in **Figure 6**. It can be seen that the pore size existing on the membrane surface does not penetrate the membrane, but only exists on the surface of the membrane, and its influence on gas permeability is negligible.
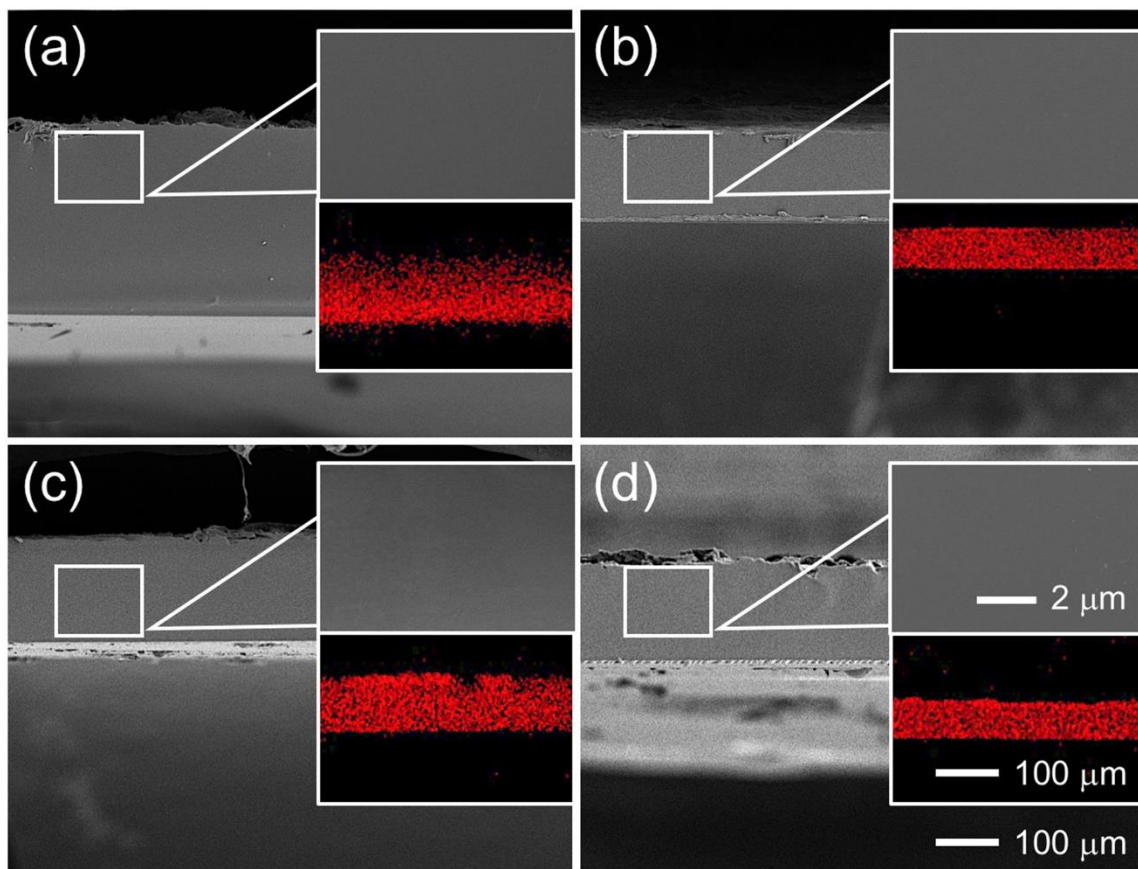

Figure 6. Cross-sectional SEM images of (a) the TB polymer precursor, (b) the CTB-600 membrane, (c) the CTB-650 membrane, and (d) the CTB-700 membrane. The scalebars in (d) apply to all the corresponding images. Associated carbon X-ray maps are included as insets.

3.6 Gas transport properties

3.6.1 Effect of carbonization temperature

The gas transport and separation properties of CMS membranes are known [42] to be strongly affected by the carbonization conditions, especially the carbonization temperature. To elucidate the temperature effect in the present series of CMS membranes, we have evaluated their transport properties by single-gas permeation tests conducted at ambient temperature with a constant feed pressure of 2 bar. The gas permeabilities of the TB precursor membrane in **Figure 7a** follow the order: $H_2 > CO_2 > N_2 > CH_4$, which complies with the order of gas kinetic diameter (2.89 Å for H_2, 3.30 Å for CO_2, 3.64 Å for N_2, and 3.80 Å for CH_4). After carbonization at a given T_c, this permeability order is retained in most cases, with the only exception being the CH_4 permeability through the CTB-500 membrane (28.7 Barrer), which is slightly higher than the N_2 permeability (11.5 Barrer). Changes in permeability for each gas species as a function of T_c, however, display greater variation. For instance, the permeabilities of CO_2, CH_4 and N_2 in **Figure 7a** first increase and then decrease with increasing T_c, exhibiting a maximum between 500 and 600 °C. During the initial stage of carbonization, oxygen and hydrogen atoms are removed from the TB polymer chains, resulting in enlarged free-volume elements and promoting a net increase in gas permeability. At later stages, the remaining chains transform to rigid aromatic carbon strands and assemble into carbon "plates." Several studies report [40, 45-47] a reduction in pore size with increasing pyrolysis temperature at constant pyrolysis time. Therefore, raising T_c can increase and subsequently decrease gas permeability, which is consistent with the changes in CO_2, CH_4 and N_2 permeability observed here.

This permeability effect is more pronounced for large gas molecules due to size sieving. For example, the largest gas examined here is CH_4 (kinetic size: 3.8 Å), which experiences an 85% reduction in permeability (from 28.7 to 4.4 Barrer) when the carbonatization temperature is increased from 500 to 600 °C. The permeabilities of the medium-size gases, such as N_2 (3.6 Å) and CO_2 (3.3 Å), however, remains nearly unchanged (11.5 to 12.6 Barrer and 376 to 366 Barrer, respectively). The smallest one, H_2 (2.8 Å), displays an unexpected trend: its permeability increases with increasing T_c. During pyrolysis, we

anticipate that the free-volume pore size increases due to the decomposition of polymer chains and subsequently shrinks as a result of carbonization. It is therefore reasonable that a maximum free-volume size exists at which gas permeability could increase with increasing T_c in the vicinity of 500-700 °C depending on the type of polymer and the size of the gas molecule. In the case of CTB pyrolyzed in this temperature range, changes in gas permeability appear to be negatively related to the kinetic size of each gas except the smallest (which can access a broader range of free-volume pores), in favorable agreement with the phenomenological mechanism proposed here. The highest permeability for H_2 in **Figure 7a** (1135 Barrer) is measured through the CTB-700 membrane, which affords a nearly 4-fold improvement compared to its TB precursor polymer. These observations agree favorably with the molecular transport expectations alluded to earlier on the basis of our results from X-ray scattering (both wide- and small-angle) and Raman spectroscopy. Similarly, gas selectivity tends to increase with increasing carbonization temperature for most of gas pairs in **Figure 7b**, although selectivity values through the CTB-500 membranes are either comparable or inferior to those measured from the TB polymer precursor. For nearly all gas pairs (except H_2/CO_2), the selectivity generally increases with increasing carbonization temperature beyond 500 °C, and such improvement is particularly evident for the H_2/N_2 and H_2/CH_4.

On one hand, the selectivity of H_2/CH_4, the gas pair with largest difference in size, in the CTB-700 membrane at ambient temperature is 1170, which is 22.4x higher than that of its precursor (50). On the other hand, the gas pair with smallest difference in kinetic sizes (CO_2/N_2) only achieves a corresponding 2.4x increase in **Figure 7b**. These results provide evidence that diffusivity selectivity dominates gas separation in these CTB membranes rather than solubility selectivity, which is consistent with molecular transport that depends mainly on molecular sieving. Simultaneous improvements in H_2 permeability and selectivity in CTB membranes result in performance levels that exceed the 2008 [48] and 2019 [49] upper bound limits, as collectively displayed in **Figure 8**. The upper bound identifies the empirical condition resulting in a trade-off between gas selectivity and gas permeability, and is commonly used to compare the gas-separation performance of membranes. The more recent 2019 upper bound is based on results reported for polymers of intrinsic porosity. In **Figures 8a-c** for gas pairs containing H_2, the CTB-700 membrane

20

consistently provides the most pronounced extent of separation improvement above the upper bound. For the CO_2/N_2 and CO_2/CH_4 pairs, however, solubility differences affect separation, and the improvements gained by the CTB-700 membrane are much less impressive than for the H_2-based pairs. The separation performance levels nevertheless reach or surpass both upper bound conditions in **Figures 8d-e**.
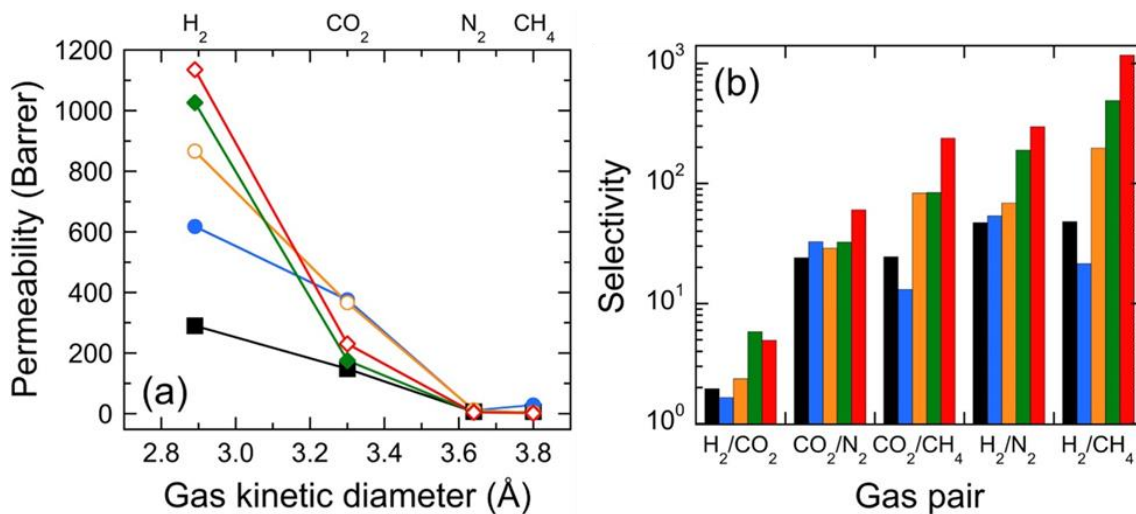

Figure 7. Measured (a) single-gas permeability and (b) ideal selectivity values of several gases and gas pairs, respectively, in the TB polymer precursor and CTB membranes prepared at different carbonization temperatures – CTB-700 (red), CTB-650 (green), CTB-600 (orange), CTB-500 (blue), and precursor (black) – as functions of gas kinetic diameter in (a) and gas pair in (b). The solid lines in (a) serve to connect the data.
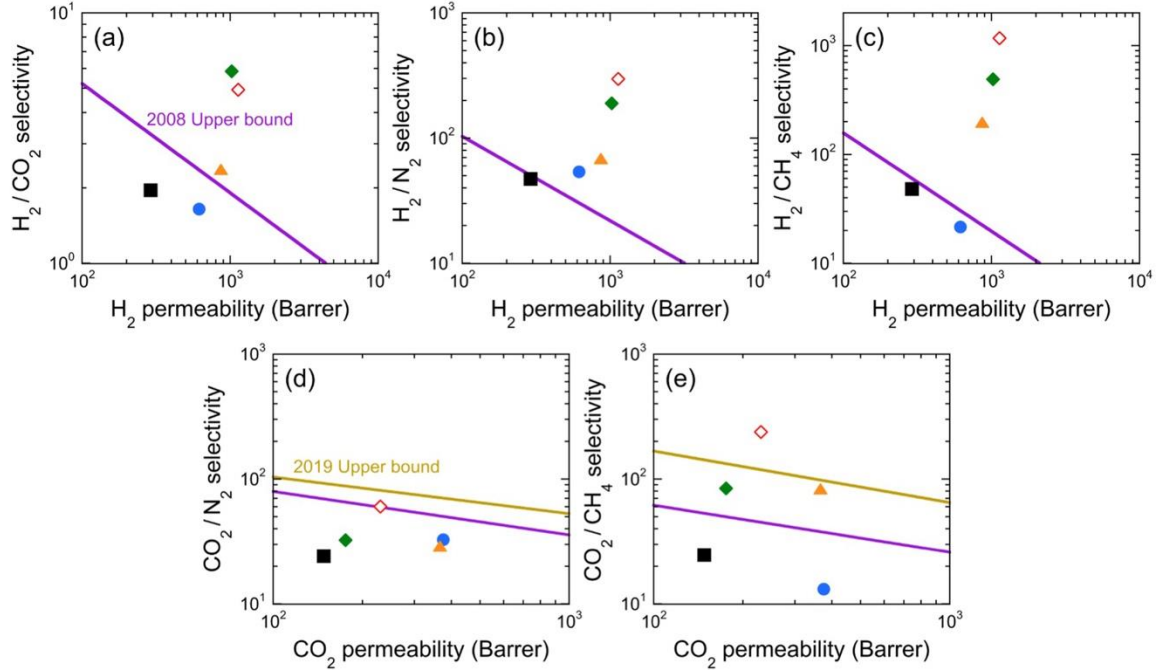
Figure 8. Gas-separation performance levels relating selectivity to H_2 permeability for (a) H_2/CO_2, (b) H_2/N_2 and (c) H_2/CH_4 gas pairs, as well as to CO_2 permeability for (d) CO_2/N_2 and (e) CO_2/CH_4 gas pairs, in the TB polymer precursor and CTB membranes prepared at different carbonization temperatures – CTB-700 (red), CTB-650 (green), CTB-600 (orange), CTB-500 (blue), and precursor (black). The 2008 [48] and 2019 [49] upper bound conditions are also provided when available.

Table 2. Separation performance of selected CMS membranes.

Materials	T_c (°C)	P_{H2} (Barrer)	P_{He} (Barrer)	$\alpha_{H2/CH4}$ (-)	$\alpha_{H2/N2}$ (-)	$\alpha_{He/CH4}$ (-)	$\alpha_{He/N2}$ (-)	refs
Matrimid®-	650	_	67.0	_	_	34.7	27.9	[16]
Kapton®	550	_	154.7	_	_	26.8	15.6	
PIM-PI	550	_	387.2	_	-	10.6	18.9	[50]
Cellulose	550	_	126.0	_	_	_	788.0	[51]
SBFDA- PI-DMN	550	_	442.0	_	_	6.1	6.7	[27]
PPO-PVP	700	1121.0	_	163.9	160.9	_	_	[52]
PEI	600	600.7	_	726.0	314.0	_	-	[53]

PI-Kapton®	950	28.1	18.1	_	2161.5	_	1392.3	[54]
PI-PABZ-6FDA	550	9495.0	_	96.0	55.5	_	_	[55]
	600	8845.0	_	147.4	85.1	_	_	
PI	800	_	58.0	_	_	206.9	121.0	[56]
PI-TB	550	14600.0	_	31.0	19.0	_	_	[28]
	650	6552.0	_	96.0	56.0	_	_	
	800	2500.0	_	200.0	66.0	_	_	
PIM-BM-TB	300	358.0	_	813.6	218.6	_	_	[57]
6F6TB	400	300.0	250.0	45.0	31.0	37.3	25.7	[58]
	450	757.0	488.0	24.0	19.0	15.7	12.2	
	400	219.0	187.0	39.0	34.0	33.3	28.7	
	450	655.0	425.0	24.0	21.0	15.7	13.7	
	400	227.0	184.0	49.0	32.0	48.3	31.5	
	450	517.0	339.0	34.0	22.0	34.4	21.5	
PIM-CANAL-TB	800	41.0	_	39.0	1952.0	_	_	[59]

3.6.2 Operating conditions

Because of its promising performance relative to the other membranes investigated here, the CTB-700 membrane has been chosen for further assessment. Since operating temperature and feed pressure constitute important process considerations, their effects on gas permeability and gas selectivity are also explored, and the results are presented in **Figures 9** and **10**, respectively. On the basis of solution-diffusion theory, an increase in temperature promotes an increase in diffusivity and a decrease in solubility, resulting in a positive activation energy of diffusion and a negative heat of sorption. Since the permeability is the product of diffusivity and solubility, the activation energy of permeation (E_P) can be positive or negative, depending on the dominant mechanism. The temperature-dependent permeabilities of the gases considered in this work through CTB-700 are

presented in **Figure 9a** and increase monotonically with increasing operating temperature from ambient temperature to 65 °C. According to **Equation 5**, values of E_P (in kJ/mol) extracted by linear regression of the data include 7.0 (H_2), 5.5 (CO_2), 19.2 (N_2), and 17.8 (CH_4). Since these E_P values are all positive, gas diffusion in the CTB-700 membrane dominates permeation. As expected on the basis of size sieving, the larger penetrant molecules possess a higher activation energy since some ultramicropores are expected to be inaccessible to these molecules and thus hinder their diffusion. Conversely, the activation energy of H_2 is higher than that of CO_2, implying that an increase in operating temperature benefits H_2/CO_2 selectivity, as confirmed in **Figure 9b**. This unexpected outcome indicates that this separation becomes more effective in high-temperature processes, such as H_2 purification following the water-gas shift reaction. For the other gas pairs, gas selectivity is observed in **Figure 9b** to decrease with increasing temperature.

In addition to operating temperature, the effect of feed pressure, ranging from 2 to 6 bar, on gas transport through the CTB-700 membrane has also been examined. According to the results provided in **Figure 10a**, an increase in feed pressure yields a reduction in the permeability (normalized to 2 bar) of all the gases investigated here. This behavior is typical of the dual-sorption mechanism [47], wherein sorption sites gradually saturate with increasing feed pressure. Previous studies have reported [40, 60, 61] that, of the gases considered here, the sorption level of H_2 in CMS membranes is the lowest, following by N_2, CH_4 and CO_2, which is largely consistent (excluding CO_2) with the inverse order of measured permeability changes observed in **Figure 10a** with regard to the CTB-700 membrane. Because H_2 permeation is the least affected by feed pressure, the corresponding H_2-based selectivities improve overall, with the H_2/CH_4 gas pair exhibiting the most promising results in **Figure 10b**. As the feed pressure is increased from 4 to 6 bar, all the selectivities are observed to decrease as a consequence of the pressure-driven losses in H_2 and CO_2 permeability. While the precise reason behind this outcome remains unclear, it remains the subject of an ongoing study. Despite reductions in gas permeability and selectivity at high feed pressure, the permeability performance of the CTB-700 membrane is still more noteworthy than most polymeric membranes, which tend to suffer from significant plasticization especially in the presence of CO_2. In addition, the selectivities of

24

H_2 and CO_2 to other gases in the CTB-700 membrane also surpass levels generally reported for polymeric membranes.
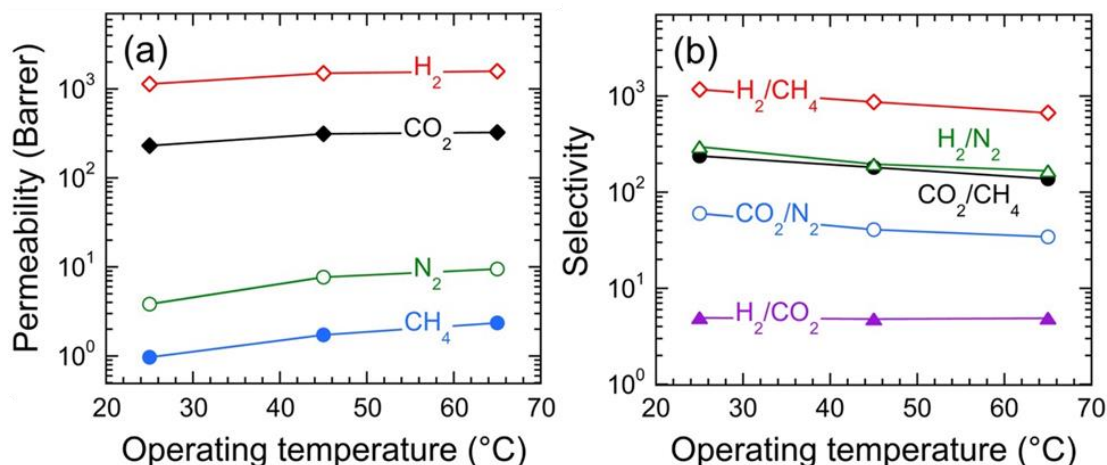

Figure 9. Measured (a) single-gas permeability and (b) ideal selectivity values of several gases and gas pairs, respectively, in the CTB-700 membrane as functions of operating temperature (see color-coded labels). The solid lines serve to connect the data.

4. Conclusions

A series of CMS membranes differing in carbonization temperature has been fabricated from a model TB polymer precursor synthesized in-house. Several physico-chemical characterization and permeation tests have been conducted to understand the effects of pyrolysis temperature on the structure and transport properties of the resulting CTB membranes. Gas permeability through these CTB membranes initially increases and then decreases with increasing pyrolysis temperature, due to a carbonization-induced change in free volume, followed by densification and a reduction in micropore size. The CTB membrane fabricated at 700 °C exhibits the most promising gas-transport performance,
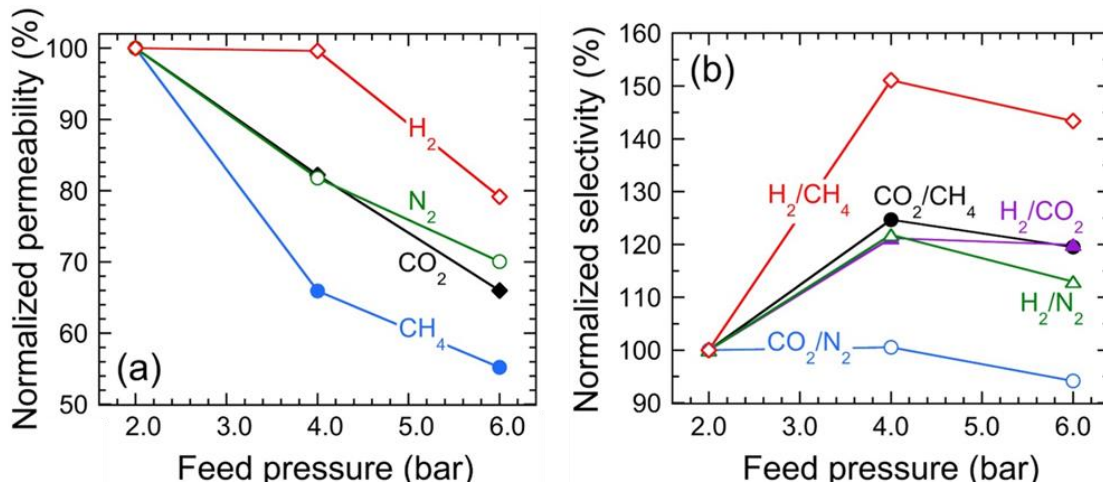
Figure 10. Normalized (a) single-gas permeability and (b) ideal selectivity values of several gases and gas pairs, respectively, in the CTB-700 membrane as functions of feed pressure (see color-coded labels). The solid lines serve to connect the data.

especially in terms of separations involving H_2. The permeability of H_2 through the CTB-700 membrane reaches 1135 Barrer at ambient temperature and a feed pressure of 2 bar, which is ~4x that of its precursor. More importantly, H_2-based selectivity levels are remarkably high, with the H_2/CH_4 selectivity reaching 1170 at ambient temperature due to the presence of narrow ultramicropores and, as a result, significant molecular sieving. These substantial improvements in H_2 transport are responsible for overall performance levels associated with H_2-related separation to exceed the upper bound conditions reported in 2008 [48] and 2019 [49].Similar, but less pronounced, separation improvement is also observed in CO_2-based separations. The effects of operating temperature and feed pressure on gas-transport properties have also been investigated for the most promising (CTB-700) membrane. Because of the dominant role of diffusion in permeation, increases in feed temperature, on one hand, promote gas permeation in CTB, especially for H_2-based separations. On the other hand, increasing feed pressure saturates sorption sites in CTB membranes, thereby decreasing gas permeability. This combination of outstanding properties makes these CTB membranes, especially CTB-700, particularly suitable for H_2-based separations, as well as potential candidates for high-temperature processes, such as H_2/CO_2 separation following the water–gas shift reaction.

Acknowledgments

References

1. Sholl, D.S. and R.P. Lively, *Seven chemical separations to change the world.* Nature, 2016. **532**(7600): p. 435-437.
2. TechNavio, *Global Gas Separation Membrane Market 2021-2025.* 2021.
3. Adams, R.T., et al., *CO2–CH4 permeation in high zeolite 4A loading mixed matrix membranes.* Journal of Membrane Science, 2011. **367**(1): p. 197-203.
4. Galizia, M., et al., *50th Anniversary Perspective: Polymers and Mixed Matrix Membranes for Gas and Vapor Separation: A Review and Prospective Opportunities.* Macromolecules, 2017. **50**(20): p. 7809-7843.
5. Lin, R., et al., *Metal organic framework based mixed matrix membranes: an overview on filler/polymer interfaces.* Journal of Materials Chemistry A, 2018. **6**(2): p. 293-312.
6. Zhang, C. and W.J. Koros, *Ultraselective Carbon Molecular Sieve Membranes with Tailored Synergistic Sorption Selective Properties.* Advanced Materials, 2017. **29**(33): p. 1701631.
7. Sanyal, O., et al., *A Self‐Consistent Model for Sorption and Transport in Polyimide‐Derived Carbon Molecular Sieve Gas Separation Membranes.* Angewandte Chemie, 2020. **132**(46): p. 20523-20527.
8. Qiu, W., et al., *Key Features of Polyimide-Derived Carbon Molecular Sieves.* Angewandte Chemie International Edition, 2021. **60**(41): p. 22322-22331.
9. Cao, Y., et al., *Carbon molecular sieve hollow fiber membranes derived from dip-coated precursor hollow fibers comprising nanoparticles.* Journal of Membrane Science, 2022: p. 120279.
10. Hu, L., et al., *Tailoring sub-3.3 A ultramicropores in advanced carbon molecular sieve membranes for blue hydrogen production.* Science Advances, 2022. **8**(10): p. eabl8160.
11. Hou, M., et al., *High-performance carbon molecular sieving membrane derived from a novel hydroxyl-containing polyetherimide precursor for CO2 separations.* Journal of Membrane Science, 2022. **656**: p. 120639.
12. Yang, Z., et al., *Benchmark CO2 separation achieved by highly fluorinated nanoporous molecular sieve membranes from nonporous precursor via in situ cross-linking.* Journal of Membrane Science, 2021. **638**: p. 119698.
13. Yu, H.J., et al., *Tailoring selective pores of carbon molecular sieve membranes towards enhanced N2/CH4 separation efficiency.* Journal of Membrane Science, 2021. **620**: p. 118814.
14. Liu, Z., et al., *Advanced carbon molecular sieve membranes derived from molecularly engineered cross-linkable copolyimide for gas separations.* Nature Materials, 2023. **22**(1): p. 109-116.
15. Araújo, T., et al., *Stable cellulose-based carbon molecular sieve membranes with very high selectivities.* Journal of Membrane Science, 2022. **641**: p. 119852.
16. Fuertes, A.B., D.M. Nevskaia, and T.A. Centeno, *Carbon composite membranes from Matrimid® and Kapton® polyimides for gas separation.* Microporous and Mesoporous Materials, 1999. **33**(1): p. 115-125.

17. Park, H.B., et al., *Relationship between chemical structure of aromatic polyimides and gas permeation properties of their carbon molecular sieve membranes.* Journal of Membrane Science, 2004. **229**(1): p. 117-127.

18. Song, C., et al., *Gas separation performance of C/CMS membranes derived from poly(furfuryl alcohol) (PFA) with different chemical structure.* Journal of Membrane Science, 2010. **361**(1): p. 22-27.

19. Pérez-Francisco, J.M., et al., *CMS membranes from PBI/PI blends: Temperature effect on gas transport and separation performance.* Journal of Membrane Science, 2020. **597**: p. 117703.

20. Steel, K.M. and W.J. Koros, *An investigation of the effects of pyrolysis parameters on gas separation properties of carbon materials.* Carbon, 2005. **43**(9): p. 1843-1856.

21. Kiyono, M., P.J. Williams, and W.J. Koros, *Effect of polymer precursors on carbon molecular sieve structure and separation performance properties.* Carbon, 2010. **48**(15): p. 4432-4441.

22. Rungta, M., et al., *Carbon molecular sieve structure development and membrane performance relationships.* Carbon, 2017. **115**: p. 237-248.

23. Xu, L., et al., *Olefins-selective asymmetric carbon molecular sieve hollow fiber membranes for hybrid membrane-distillation processes for olefin/paraffin separations.* Journal of Membrane Science, 2012. **423-424**: p. 314-323.

24. Vu, D.Q., W.J. Koros, and S.J. Miller, *High pressure CO_2/CH_4 separation using carbon molecular sieve hollow fiber membranes.* Industrial & engineering chemistry research, 2002. **41**(3): p. 367-380.

25. Fu, Y.-J., et al., *Adjustable microstructure carbon molecular sieve membranes derived from thermally stable polyetherimide/polyimide blends for gas separation.* Carbon, 2017. **113**: p. 10-17.

26. Ma, X., et al., *Carbon molecular sieve gas separation membranes based on an intrinsically microporous polyimide precursor.* Carbon, 2013. **62**: p. 88-96.

27. Hazazi, K., et al., *Ultra-selective carbon molecular sieve membranes for natural gas separations based on a carbon-rich intrinsically microporous polyimide precursor.* Journal of Membrane Science, 2019. **585**: p. 1-9.

28. Wang, Z., et al., *Carbon Molecular Sieve Membranes Derived from Tröger's Base-Based Microporous Polyimide for Gas Separation.* ChemSusChem, 2018. **11**(5): p. 916-923.

29. Ye, C., et al., *Fine tune gas separation property of intrinsic microporous polyimides and their carbon molecular sieve membranes by gradient bromine substitution/removal.* Journal of Membrane Science, 2023. **669**: p. 121310.

30. Deng, J., Z. Dai, and L. Deng, *H2-selective Troger's base polymer based mixed matrix membranes enhanced by 2D MOFs.* Journal of Membrane Science, 2020. **610**: p. 118262.

31. Fan, Y., et al., *Tröger 's base mixed matrix membranes for gas separation incorporating NH2-MIL-53(Al) nanocrystals.* Journal of Membrane Science, 2019. **573**: p. 359-369.

32. Cosey, W.K., et al., *Reduced Aging in Carbon Molecular Sieve Membranes Derived from PIM-1 and MOP-18.* Industrial & Engineering Chemistry Research, 2021. **60**(27): p. 9962-9970.

33. Lagorsse, S., F.D. Magalhães, and A. Mendes, *Aging study of carbon molecular sieve membranes.* Journal of Membrane Science, 2008. **310**(1): p. 494-502.

34. Ma, X., et al., *Propylene/Propane Mixture Separation Characteristics and Stability of Carbon Molecular Sieve Membranes.* Industrial & Engineering Chemistry Research, 2015. **54**(40): p. 9824-9831.

35. Shao, L., T.-S. Chung, and K.P. Pramoda, *The evolution of physicochemical and transport properties of 6FDA-durene toward carbon membranes; from polymer, intermediate to carbon.* Microporous and Mesoporous Materials, 2005. **84**(1): p. 59-68.

36. Du, F., et al., *Nitrogen-doped carbon dots with heterogeneous multi-layered structures.* RSC Advances, 2014. **4**(71): p. 37536-37541.

37. Delhaes, P., *Graphite and precursors.* Vol. 1. 2000: CRC Press.

38. Allen, M.J., V.C. Tung, and R.B. Kaner, *Honeycomb Carbon: A Review of Graphene.* Chemical Reviews, 2010. **110**(1): p. 132-145.

39. Qiu, W., et al., *Hyperaging Tuning of a Carbon Molecular-Sieve Hollow Fiber Membrane with Extraordinary Gas-Separation Performance and Stability.* Angewandte Chemie International Edition, 2019. **58**(34): p. 11700-11703.

40. Rungta, M., L. Xu, and W.J. Koros, *Structure–performance characterization for carbon molecular sieve membranes using molecular scale gas probes.* Carbon, 2015. **85**: p. 429-442.

41. Ma, Y., et al., *Creation of Well-Defined "Mid-Sized" Micropores in Carbon Molecular Sieve Membranes.* Angewandte Chemie International Edition, 2019. **58**(38): p. 13259-13265.

42. Lei, L., et al., *Carbon membranes for CO2 removal: Status and perspectives from materials to processes.* Chemical Engineering Journal, 2020. **401**: p. 126084.

43. Short, M.A. and P.L. Walker, *Measurement of interlayer spacings and crystal sizes in turbostratic carbons.* Carbon, 1963. **1**(1): p. 3-9.

44. Chen, T., et al., *High CO2 permeability of ceramic-carbonate dual-phase hollow fiber membrane at medium-high temperature.* Journal of Membrane Science, 2020. **597**: p. 117770.

45. Ning, X. and W.J. Koros, *Carbon molecular sieve membranes derived from Matrimid® polyimide for nitrogen/methane separation.* Carbon, 2014. **66**: p. 511-522.

46.   Sanyal, O., et al., *Next generation membranes —using tailored carbon.* Carbon, 2018. **127**: p. 688-698.
47.   Lei, L., et al., *Carbon hollow fiber membranes for a molecular sieve with precise-cutoff ultramicropores for superior hydrogen separation.* Nature Communications, 2021. **12**(1): p. 268.
48.   Robeson, L.M., *The upper bound revisited.* Journal of Membrane Science, 2008. **320**(1): p. 390-400.
49.   Comesaña-Gándara, B., et al., *Redefining the Robeson upper bounds for CO2/CH4 and CO2/N2 separations using a series of ultrapermeable benzotriptycene-based polymers of intrinsic microporosity.* Energy & Environmental Science, 2019. **12**(9): p. 2733-2740.
50.   Ogieglo, W., et al., *Thin Composite Carbon Molecular Sieve Membranes from a Polymer of Intrinsic Microporosity Precursor.* ACS Applied Materials & Interfaces, 2019. **11**(20): p. 18770-18781.
51.   Rodrigues, S.C., et al., *Preparation of carbon molecular sieve membranes from an optimized ionic liquid-regenerated cellulose precursor.* Journal of Membrane Science, 2019. **572**: p. 390-400.
52.   Itta, A.K., H.-H. Tseng, and M.-Y. Wey, *Fabrication and characterization of PPO/PVP blend carbon molecular sieve membranes for H2/N2 and H2/CH4 separation.* Journal of Membrane Science, 2011. **372**(1): p. 387-395.
53.   Tseng, H.-H., et al., *Enhanced H2/CH4 and H2/CO2 separation by carbon molecular sieve membrane coated on titania modified alumina support: Effects of TiO2 intermediate layer preparation variables on interfacial adhesion.* Journal of Membrane Science, 2016. **510**: p. 391-404.
54.   Suda, H. and K. Haraya, *Gas Permeation through Micropores of Carbon Molecular Sieve Membranes Derived from Kapton Polyimide.* The Journal of Physical Chemistry B, 1997. **101**(20): p. 3988-3994.
55.   Liang, J., et al., *Effects on Carbon Molecular Sieve Membrane Properties for a Precursor Polyimide with Simultaneous Flatness and Contortion in the Repeat Unit.* ChemSusChem, 2020. **13**(20): p. 5531-5538.
56.   Fuertes, A.B. and T.A. Centeno, *Carbon molecular sieve membranes from polyetherimide.* Microporous and Mesoporous Materials, 1998. **26**(1): p. 23-26.
57.   Chen, X., et al., *Ultra-selective molecular-sieving gas separation membranes enabled by multi-covalent-crosslinking of microporous polymer blends.* Nature Communications, 2021. **12**(1): p. 6140.
58.   Hu, X., et al., *Thermally rearranged polybenzoxazole copolymers incorporating Tröger's base for high flux gas separation membranes.* Journal of Membrane Science, 2020. **612**: p. 118437.
59.   Hazazi, K., et al., *Catalytic arene-norbornene annulation (CANAL) ladder polymer derived carbon membranes with unparalleled hydrogen/carbon dioxide size-sieving capability.* Journal of Membrane Science, 2022. **654**: p. 120548.
60.   Xu, R., et al., *Ultraselective carbon molecular sieve membrane for hydrogen purification.* Journal of Energy Chemistry, 2020. **50**: p. 16-24.
61.   Omidvar, M., et al., *Unexpectedly Strong Size-Sieving Ability in Carbonized Polybenzimidazole for Membrane H2/CO2 Separation.* ACS Applied Materials & Interfaces, 2019. **11**(50): p. 47365-47372.